Materials and Design 200 (2021) 109438

Contents lists available at ScienceDirect

Materials and Design

journal homepage: www.elsevier.com/locate/matdes

Sensitivity of material failure to surface roughness: A study on titanium alloys Ti64 and Ti407

Scott Sneddon [a,*], Yang Xu [a], Mark Dixon [b], David Rugg [b], Peifeng Li [a], Daniel M. Mulvihill [a,*]

[a] James Watt School of Engineering, University of Glasgow, Glasgow G12 8QQ, UK
[b] Rolls-Royce plc, PO Box 31, Derby DE24 8BJ, UK

HIGHLIGHTS

- Investigates the effect of surface finish on failure behaviour of two key aerospace titanium alloys: Ti64 and Ti407.
- Failure strain (and work-to-failure) in Ti64 is highly sensitive to both magnitude and orientation of surface roughness.
- High roughness in max tensile stress direction (& scratches perpendicular to this direction) were most detrimental.
- Cracks initiate at zones of high plastic strain at tips of roughness valleys corresponding to high local surface curvature.
- Ti407 was insensitive to surface roughness (even up to Ra = 20 μm) owing to its significantly greater ductility.

GRAPHICAL ABSTRACT

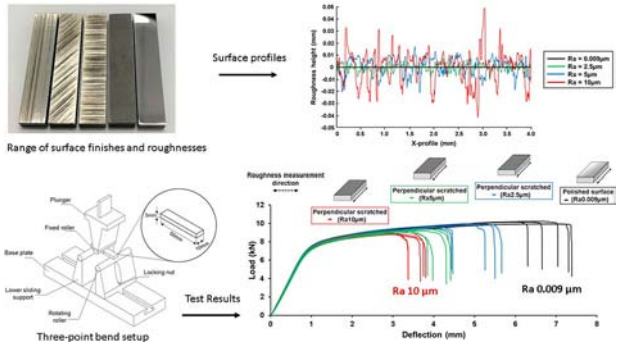

ARTICLE INFO

Article history:
Received 20 October 2020
Received in revised form 7 December 2020
Accepted 21 December 2020
Available online 29 December 2020

Keywords:
Surface roughness
Ti407
Ti64
Material failure
Crack propagation
Titanium alloys

ABSTRACT

The relationship between material failure and surface roughness has been investigated using two titanium alloys: Ti64 and the more ductile Ti407. Three surface types were created (polished, sandblasted and scratched) with instances spanning a wide range of average roughness. The surfaces were tested in three-point bending with the imparted roughness on the tensile under-surface of a rectangular beam specimen. Results showed failure of Ti64 to be highly sensitive to both magnitude and orientation of roughness. High roughness in the maximum tensile stress direction (and scratch like features perpendicular to this direction) were most detrimental. Thus, strain-to-failure (and work-to-failure) in Ti64 dropped off significantly with increasing surface roughness in the tensile direction. Finite element modelling of the test indicated that cracks initiate at zones of high plastic strain at the tips of roughness valleys due to high local surface curvature. Thus, roughness can be considered as a series of blunt crack-like features where larger crack tip curvature induces greater likelihood of crack propagation. Contrastingly, the mechanical response of Ti407 was insensitive to surface roughness owing to its significantly greater ductility. Thus, designers need to be aware of the sensitivity of failure of particular materials to surface roughness. The insensitivity of Ti407 is advantageous, but the sensitivity of failure to surface roughness in a material like Ti64 is potentially serious if not properly accounted for.

* Corresponding authors.
E-mail addresses: s.sneddon.1@research.gla.ac.uk (S. Sneddon), Daniel.Mulvihill@glasgow.ac.uk (D.M. Mulvihill).

https://doi.org/10.1016/j.matdes.2020.109438

1. Introduction

How sensitive is material failure in metal alloys to surface roughness and what material properties govern the relationship? The issue is important because high sensitivity to roughness would mean incurring extra machining costs in guaranteeing potentially low levels of roughness and it could also leave in-service parts with surface damage susceptible to failure. Insensitivity to roughness, on the other hand, would permit a greater range of safe surface finishes and less susceptibility to failure due to surface damage. Here, we investigate this question using two titanium alloys: the current industry standard Ti64 (Ti-6Al-4 V) and the newly developed (and more ductile) Ti407 alloy (Ti-0.85Al-3.9 V-0.25Si-0.25Fe).

Titanium alloys are widely used in the aerospace sector owing to their attractive mechanical and corrosion-resistant properties [1,2]. Such alloys are found in applications where a combination of excellent strength, toughness and surface integrity are required. The surface integrity of titanium alloys has been found to play a key role in the reduction of surface stress concentrations and subsequently, provide a longer in-service lifespan of components [3,4]. However, due to several inherent properties including low thermal conductivity, elastic modulus and poor chemical reactivity, machining titanium alloys is laborious and expensive [3,5]. It is thought that more ductile titanium alloys may offer improved surface integrity and ease of machining. Two-phase α/β titanium alloys find use in a variety of sectors including aerospace, biomedical and energy applications. Ti64 is well established as the workhorse α/β titanium alloy for aerospace applications through its inherently good balance of energy absorption and strength to weight ratio [6]. In applications where toughness is a key requirement, reliable surface integrity is needed to ensure consistent mechanical properties. Poor surface integrity can cause high machining costs, surface defects, initiate cracks and cause premature failure in metallic components [7]. Despite the attractive properties associated with Ti64, considerable time and costs are invested to achieve the desired surface finish for its application. Ti407 is a newly developed titanium alloy in the α/β series specifically designed for reduced manufacturing costs and applications involving increased energy absorption and good surface integrity [8]. Ti407 diverges from the common Ti64 composition though a reduction in aluminium content, producing a high-ductility alloy with medium-strength characteristics [9]. Reduced solute atom strengthening is the driving mechanism for these characteristic changes. Reduced aluminium content has been shown to significantly decrease the strength properties of titanium alloys [10]. The reduced solute atom strengthening in Ti407 provides desirable opportunities for improved machinability and impact performance, in contrast to Ti64. Ti407, like Ti64, is a two-phase titanium alloy consisting of a primary aluminium-stabilised alpha-phase and a secondary vanadium-stabilised beta-phase [9,11]. The microstructures consist of a primary alpha-phase of ≈90–95% hexagonal close-packed unit cell and a secondary beta-phase ≈ 5–10% body-centred cubic unit cell. Sneddon et al. [12] compared the bulk tensile and compressive mechanical behaviour of both alloys and found that Ti407 was considerably more ductile. The increased ductility of Ti407 should provide opportunities for an improved strain to failure under monotonic loading and better accommodation of surface stress concentrations.

The effect of surface roughness on failure in Ti64 has been studied mostly in relation to fatigue performance [13,14]. The various studies indicate that fatigue life reduces with increased surface roughness since roughness provides stress concentration sites capable of inducing crack nucleation. Much more work has been carried out on the roughness dependent fatigue properties of steels [15–18] where similar conclusions have been made (i.e. increasing roughness reduces both fatigue life and fatigue strength). However, there appears to be surprisingly less work available on the effect of roughness upon failure in monotonic loading. Failure mechanisms in titanium are usually discussed in relation to subsurface microstructural behaviour and several advanced models are available for predicting the resulting bulk failure [19–21]. The material's inherent microstructure can give rise to variations in grain size, grain texturing and include the presence of macro-zones [12]. These can act as a differential to promote failure in such alloys under an applied load. It is widely known, for example, that reduced grain size in metallic materials results in improved crack initiation resistance via the Hall-Petch relationship [22]. The texturing of Ti-alloys has also been directly linked to failure with directional strength attributed to loads applied parallel to the c-axis of the HCP unit cell [2] and the presence of macro-zones can also be a driving force for pre-mature subsurface failure mechanisms [23].

While much effort has been invested in models to predict bulk failure based on microstructural phenomenon, rather little is known about the effect of varying degrees of surface roughness on failure and how this might be modelled. If surface roughness plays an important role, then models based solely on bulk microstructural behaviour could potentially be highly inaccurate and careful attention would have to be given to surface finish in the machining of critical components which would inevitably increase machining costs. Therefore, this question of the effect of surface finish upon failure in a very important one with widespread implications for the design of safety-critical components, not just in titanium alloys but across the metal alloys. Before concerning ourselves with predictive models, we first need to assess the importance of surface roughness in the failure process. This paper comprehensively characterises the effect of surface roughness on the failure behaviour of Ti64 and the more ductile Ti407. Quasi-static three-point bend tests on samples having a wide range of known surface roughness values were used to determine the effect of roughness on the macroscopic mechanical response as the samples were tested to failure. The results indicate that failure strain (and hence, energy absorption) is highly sensitive to surface roughness for Ti64. Interestingly, Ti407 was too ductile to fail even at maximum deflection and hence the mechanical responses we obtained for Ti407 were essentially insensitive to surface finish. A finite element model is also developed to replicate the experimental roughness profiles and attempt to understand the mechanism by which roughness can govern failure strain (i.e. as in Ti64).

2. Experimental approach

2.1. Materials

Materials were supplied by Rolls-Royce plc and manufactured by Timet. Ti64 and Ti407 were supplied in plate form (approx. 50 cm^2 & 20 cm^2, respectively and of thickness 14–16 cm). The Ti64 plate was produced by melting with an electron beam (EB) via cold hearth furnace followed by vacuum arc re-melt (VAR) to produce an ingot. Ingot open die forging using a combination of beta working and alpha-beta working produced an intermediate plate. The plate was then UD rolled in the alpha-beta phase-field followed by a creep flattening procedure. The Ti407 plate was produced by electron beam single melt (EBSM) via cold hearth furnace to create an ingot. The Ti407 material was forged above the beta transus from an ingot through a square cross-section. The piece was then cross-rolled in the alpha-beta phase field to a rectangular cross-section. The material was solution heat-treated and aged (STA). Details of each alloy composition are listed in Table 1.

Table 1
Ti64 and Ti407 composition and physical properties [9].

Material	Al (wt%)	V (wt%)	O (wt%)	Si (wt%)	Fe (wt%)	ρ (g/cm^{-3})	T_β °C
Ti64	6.0	4.0	0.15	–	0.15	4.42	996
Ti407	0.85	3.90	0.15	0.25	0.25	4.53	887

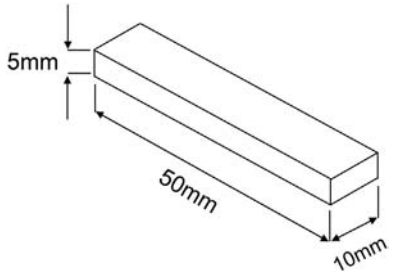

Fig. 1. Three-point bend specimen dimensions.

2.2. Surface finish and preparation

Titanium three-point bend specimens were manufactured via wire electrical discharge machining (EDM) in the rolling direction (RD) to produce the three-point bend samples shown in Fig. 1. Wire EDM was selected to maintain dimensional accuracy across all specimens and minimise deformation of the surfaces.

Three surface types were produced for the study: polished, unidirectional scratched (similar to a ground surface) and sandblasted. The imposed surface finishes were applied to the underside of the beam only (i.e. the tensile surface in three-point bending). The polished surface was selected as the benchmark minimum roughness sample. The unidirectional scratched surface allows us to easily create a range of different roughnesses and to assess the effect of scratch depth and orientation on failure. Lastly, the sandblasted surface provides a comparison with the result of an isotropic randomly rough surface.

The polished surface was prepared through the traditional three-stage grinding and polishing procedure using Struers Cito-Press and Labo-force-50: Initial coarse grinding with a diamond disc, fine grinding with composite pad and diamond suspension, followed by a chemical/mechanical polish with neoprene pad and colloidal silica solution. The polishing process produced a nominal Ra of ~0.009 μm. The sandblasted surfaces were produced using a fully enclosed sandblaster with 60 grade (0.4 mm approx.) aluminium oxide particles until the wire eroded surface finish was removed. An isotropic, micro-pitted surface was obtained with nominal Ra of approx. 4 μm. Three different instances of the unidirectional scratched surface type were produced depending on the orientation of the scratches relative to the beam longitudinal axis: perpendicular scratched, parallel scratched and 45° scratched. Fig. 2 shows the main surface types produced. Unlike the polished and sandblasted samples, unidirectional scratched samples were produced at three different nominal roughness levels: ~2.5 μm, ~5 μm and ~ 10 μm. For Ti407, a fourth unidirectional scratched surface having Ra ~ 20 μm was produced. Two different grades of silicon carbide abrasive paper (3M P40 and JFlex P26) were required to produce the 2.5 μm and 5 μm surfaces. To achieve consistent perpendicular and parallel abraded surfaces, a 3D printed mould was designed to encase each sample during the scratching process (see Fig. 3). Scratches were applied by manually exerting force on the samples in a linear motion using the straight edge as a guide. A diamond-tipped scribe was used to achieve the 10 & 20 μm scratched roughnesses (too high for most commercial abrasive paper). A summary of the nominal target roughness produced by each surface preparation method is shown in Table 2 (Note, for the unidirectional scratched surfaces, the nominal Ra values are always measured perpendicular to the scratches). Although actual roughness measurements will differ somewhat from Table 2, these nominal values are used to designate the different roughness cases in the remainder of the paper.

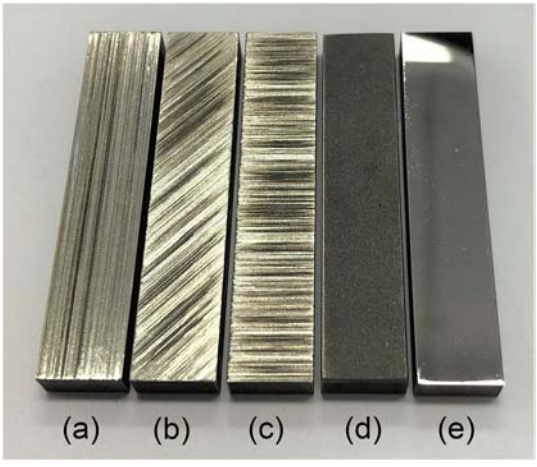

Fig. 2. Photo of surface finishes: (a) Parallel scratched, (b) 45° scratched, (c) perpendicular scratched, (d) sandblasted and (e) polished.

2.3. Surface characterisation

The topography of each surface was characterised with an Alicona Infinite Focus profilometer using a x10 objective. For each sample, 10 line profile scans were taken (each) in the longitudinal and transverse directions (the Ra(x) and Ra(y) directions in Fig. 4) to produce an average Ra (mean surface profile roughness) value for each direction. A surface texture scan Sa (mean surface area roughness) was also taken for a larger area highlighted in yellow. The line profile scans were 4 mm in length and complied with ISO 4288-1996 (i.e. in relation to cut-off wavelength λ_c). The surface texture scan was conducted over an area of 7 mm^2 at matching resolution to the previous scans. The line profile scans highlight directional roughness in the x and y directions while the surface texture scan (Sa) reports a single roughness value for a specified region. The centre of all scans coincided with the middle of the beam width at mid-span so that roughness measurements coincide with the region of maximum tensile stress during three-point bending.

Since maximum tensile stress acts in the longitudinal (i.e. x-direction) in three-point bending, the Ra(x) values are likely to be more indicative of failure behaviour than either Ra(y) or Sa. A comparative plot showing Ra (x) on Ti64 samples for the polished surface (Ra 0.009 μm) and the three perpendicular scratched surfaces with Ra 2.5, 5 and 10 μm is shown in Fig. 5. The range of 0.009 (polished) to 10 μm (very rough) represents a comprehensive range as it encompasses the majority of practical engineering surface roughness possibilities.

The measured average roughness values for the longitudinal direction Ra(x) are summarised in Table 3 for Ti64 and Table 4 for Ti407. These represent the average of 50 scans (10 on each of 5 samples of each surface condition). Unsurprisingly, the Ra measured along the scratches (i.e. Ra(x) for Parallel scratched samples) is substantially less than for across the same scratch type (i.e. Ra(x) for Perpendicular

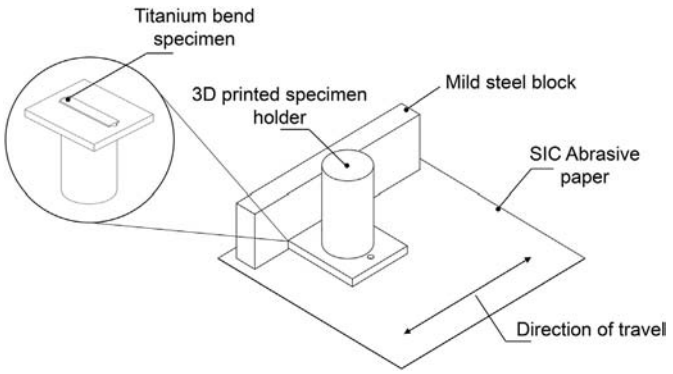

Fig. 3. Fixture for abrading parallel and perpendicular scratched surfaces.

Table 2
Nominal (target) Ra produced by each surface preparation method. For the unidirectional surfaces, the nominal Ra is always measured perpendicular to the scratches.

Method	Polish	P40 abrasive	20 μm sandblasted	P26 abrasive	P26 abrasive + scribing	P26 abrasive + scribing
Nominal Designation	Polished	Unidirectional Scratched Ra2.5	Sandblasted	Unidirectional Scratched Ra5	Unidirectional Scratched Ra10	Unidirectional Scratched Ra20
Nominal Roughness (Ra)	≈ 0.009 (μm)	≈ 2.5 (μm)	≈ 4.0 (μm)	≈ 5.0 (μm)	≈ 10 (μm)	≈ 20 (μm)

scratched). The directionality of the surface features may play an important role in influencing failure initiation. In this case, Ra would be a better descriptor as Sa is unable to distinguish directionality.

2.4. Three-point bend testing

The three-point bend experimental work was conducted on an Instron 2530-30kN equipped with a three-point bend rig. The bending apparatus was adapted from a design provided by Dr. Z. Liu (see Acknowledgements) with free-moving rollers to reduce friction during the test. The rig was manufactured from tool steel with hardened and ground roller bars of a radius 5 mm. The fixture separation spans 15-170 mm with a max deflection of 50 mm. For specimen dimensions, 50 ×10 ×5 mm, a fixture separation of 25 mm was calculated from ATSM E290-14. The three-point bend setup is displayed in Fig. 6. To record and analyse strain and fracture events during bending, a Pixelink PL-D732MU-T USB camera with a Navatar lens was mounted on a level tripod and set up to image the side of the specimen during testing. Biaxial three-point bend experiments were performed to ATSM E290-14. A quasi-static strain rate was used to displace the plunger axially at a constant 0.005 mm/s^{-1} resulting in a strain rate of $\dot{\varepsilon}$=0.001 s^{-1}. For each condition, the bend rig and lower roller supports were static while the upper grip monotonically displaced the plunger at the specified strain rate until failure or maximum deflection was reached. Rotation was observed in the lower rollers to indicate reduced friction between the sample and roller during each test. Displacement was measured though cross-head displacement until failure while strain on the side of the specimens was determined from the videos recorded by the camera.

While plunger displacement is obtained directly from the crosshead displacement, inelastic strain beyond small deflections cannot be calculated from this and must be determined experimentally. To obtain strain, side-on images of the specimen were recorded during deformation at 2 fps using the Pixelink camera with an external lighting source. Strain was then determined as the *average* strain over a 6 mm line segment positioned at the outer tensile surface at mid-span. This was done using ImageJ by tracking the extension (at the tensile surface) between two black lines marked 6 mm apart on the specimen. While this value will be less than the pointwise local maximum strain close to mid-span, trends in relation to surface roughness will be equivalent. Fig. 7 shows a Ti64 specimen (with the black lines) at three stages of deformation.

The bend specimens were displaced until failure occurred or until maximum deflection was reached. Plunger force, plunger displacement and tensile strain data were determined during loading. The test was carried out for each surface condition listed in Tables 3 and 4 and all tests were repeated five times.

3. Experimental results

3.1. Ti64 results

3.1.1. Initial results

The first set of Ti64 results to emerge from the study are plotted in Fig. 8. Force is plotted against deflection for a selection of the surface types: perpendicular scratched Ra 2.5 μm, parallel scratched Ra 2.5 μm, sandblasted Ra 4 μm and polished, Ra 0.009 μm. The five repeat tests for each surface type are plotted. We can clearly see that the failure of the polished samples is delayed to greater deflection values than for the rougher scratched and sandblasted cases. The figure also suggests that the orientation of surface features plays an important role. Although the sandblasted specimens (isotropic in terms of surface directionality) are considerably rougher (Ra 4 μm) than the perpendicular scratched specimens (Ra 2.5 μm), there is little difference between their maximum deflections (see the values in Table 5) and the two samples failing at the lowest deflection values (in Fig. 8) are actually perpendicularly scratched. We also see that the perpendicularly scratched samples failed at lower deflections than the parallel scratched samples even though the nominal roughness level across the scratches is exactly the same in each case (i.e. 2.5 μm). Fig. 8, therefore, indicates that the perpendicular scratched scenario (i.e. scratches perpendicular to the tensile stress direction) is the most detrimental in terms of failure. This makes sense if one imagines surface roughness as a series of blunt crack-like features on a surface (see Fig. 9). Longer cracks (i.e. akin to scratches) are likely to be easier to propagate, than, for example, the micro-pits on a sandblasted surface and cracks orientated perpendicularly to the greatest tensile stresses are likely to most detrimental. This is equivalent to the perpendicular scratches here as these are perpendicular to the maximum tensile stresses due to bending on the outer surface. Note, that the sharpness of the crack-like features in the roughness profile in Fig. 9 is exaggerated as the height axis is always magnified in these plots (the enlarged valley profile in Fig. 9 would be more representative).

Table 5 summarises the average deflection to failure and work to failure, for the tests graphed in Fig. 8. It is clear that, when these surface

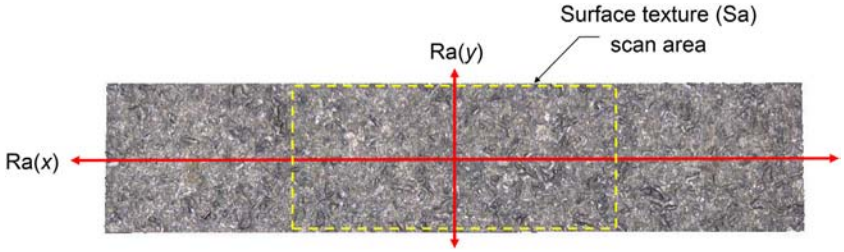

Fig. 4. Regions and directions for surface roughness measurements (sandblasted).

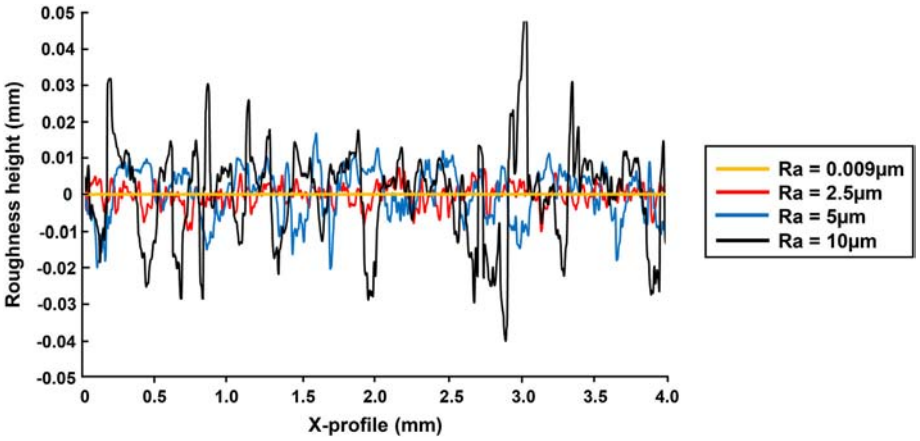

Fig. 5. Longitudinal Surface roughness profiles (i.e. *x*-direction) for Ti64 polished and perpendicular scratched samples.

Table 3
Ti64 average longitudinal surface roughness Ra(*x*) and areal surface roughness (Sa) values. Values are average from 10 scans on all five samples of each (i.e. 50 scans). Plus/minus (±) values are standard deviations.

Condition	Ra(*x*) (μm)	Sa (μm)
Polished	0.009 ± 0.002	0.026
Parallel Scratched Ra2.5	1.09 ± 0.61	2.65
Perpendicular Scratched Ra2.5	2.44 ± 0.37	2.62
Sandblasted	3.91 ± 0.34	4.45
Perpendicular Scratched Ra5	5.04 ± 0.36	5.14
45° Scratched Ra10	8.38 ± 1.01	10.20
Parallel Scratched Ra10	1.73 ± 0.54	10.24
Perpendicular Scratched Ra10	10.01 ± 0.49	10.25

Table 4
Ti407 average longitudinal surface roughness Ra(*x*) and areal surface roughness (Sa) values. Values are average from 10 scans on all five samples of each (i.e. 50 scans). Plus/minus (±) values are standard deviations.

Condition	Ra (*x*) (μm)	Sa (μm)
Polished	0.009 ± 0.002	0.026
Perpendicular Scratched Ra2.5	2.45 ± 0.18	2.60
Perpendicular Scratched Ra5	4.91 ± 0.06	4.96
Perpendicular Scratched Ra10	9.96 ± 0.33	9.88
Perpendicular Scratched Ra20	19.60 ± 0.96	20.56

types are listed in order of decreasing Ra (*x*), an increasing trend is observed for deflection and work to failure. This indicates that failure is strongly related to Ra (*x*) (i.e. roughness measured in the tensile stress direction); whereas, measures like Sa fail to distinguish the directional difference between the perpendicular and parallel instances of the nominal 2.5 μm roughness.

3.1.2. Effect of surface roughness magnitude

In light of Fig. 8, it was decided to study the effect of varying the roughness magnitude (in the maximum tensile stress direction) of a single surface type. The perpendicularly scratched case was chosen as this is likely to be the most detrimental for failure. Fig. 10 plots force versus deflection for perpendicular scratched roughnesses of 2.5, 5 and 10 μm and compares these to the polished 0.009 μm result. Again the graph plots five repeats for each test and the average deflection and work to failure values for each case are given in Table 6 along with measured roughness. Fig. 10 and Table 6 indicate a very distinctive trend whereby deflection and work to failure reduce dramatically with increasing surface roughness.

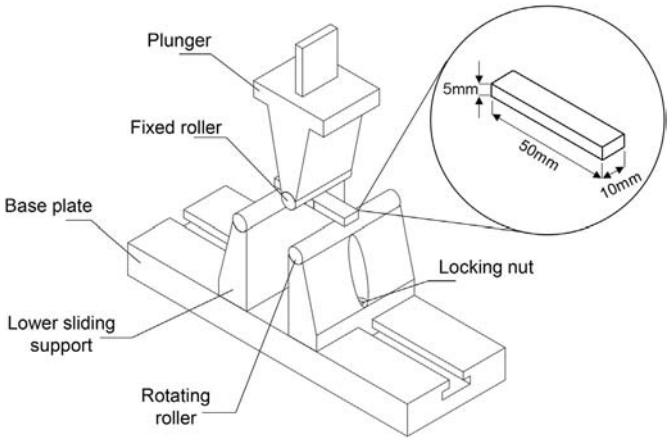

Fig. 6. Three-point bend test setup.

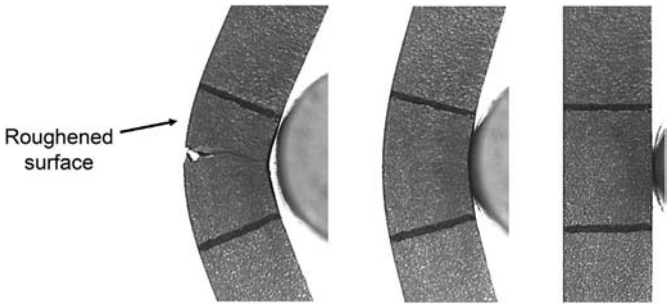

Fig. 7. Stages of three-point bend deformation of a Ti64 specimen.

The key implication here is that a very wide range of failure deflections (and hence work to failure values) are possible depending on the severity of the surface roughness. Going from the 0.009 μm polished surface to the 10 μm scratched surface, deflection to failure dropped off by almost a factor of 2 and work to failure reduced 2.7 times. Maximum load (and by extension maximum stress) also decreased, but the effect here was less significant (a reduction of 1.1 times) as Ti64 has a low strain hardening gradient. Returning to the blunt crack analogy for surface roughness (Fig. 9), it makes sense that deeper (i.e. sharper) scratches will induce failure sooner. For example, the roughness troughs (or crack tips) on the deeply scratched surfaces would be expected to

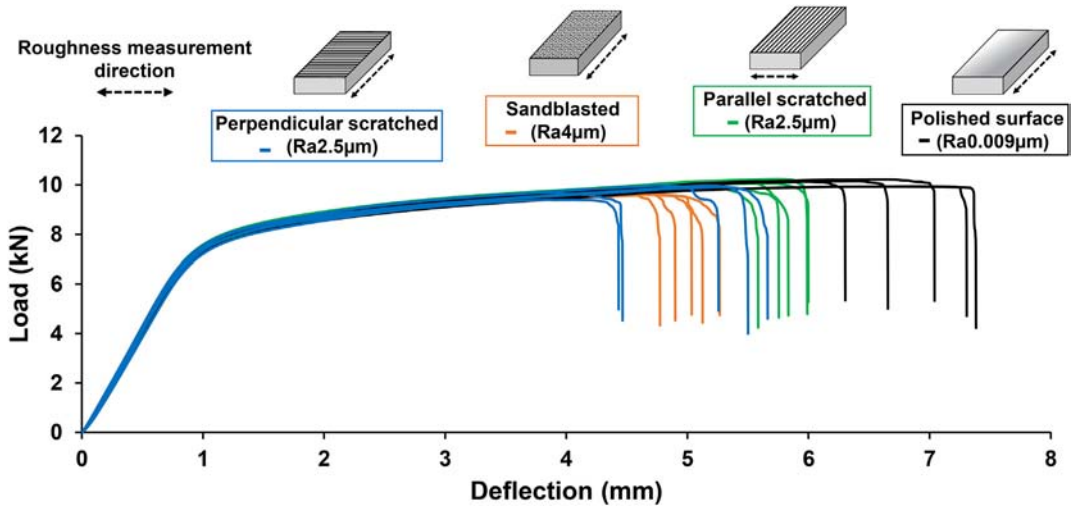

Fig. 8. Ti64 force-displacement curves for polished Ra 0.009 μm (black), sandblasted Ra 4 μm (orange), perpendicular scratched Ra 2.5 μm (blue) and parallel scratched Ra 2.5 μm (green). Five repeat test results are shown for each. (For interpretation of the references to colour in this figure legend, the reader is referred to the web version of this article.)

Table 5
Average deflection to failure and average work to failure (with measured mean roughness Ra & Sa) for the selection of Ti64 surface types graphed in Fig. 8. Plus/minus (±) values are standard deviations.

Surface condition	Ra (x) (μm)	Sa (μm)	Max load (kN)	Deflection to failure (mm)	Work to failure (J)
Sandblasted (Ra 4 μm)	3.91	4.35	9.66 ± 0.05	5.02 ± 0.17	20,710.58 ± 671.78
Perpendicular scratched (Ra 2.5 μm)	2.44	2.62	9.74 ± 0.20	5.09 ± 0.56	20,989.47 ± 2591.33
Parallel scratched (Ra 2.5 μm)	1.73	2.65	10.03 ± 0.14	5.83 ± 0.16	25,204.97 ± 1040.96
Polished (Ra 0.009 μm)	0.008	0.03	10.08 ± 0.12	6.94 ± 0.41	30,716.37 ± 1823.40

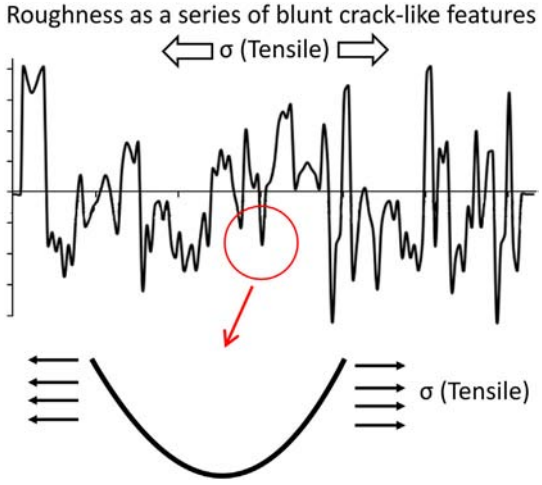

Fig. 9. Surface roughness as a series of blunt crack-like features (shown here in tension).

have a greater curvature magnitude than the troughs on the polished surface (this is even clear from the profiles in Fig. 5) and hence stress intensity at the tip of the rougher features can be expected to be much higher; thereby initiating crack propagation sooner – we examine this further in Section 4. In-situ images of surface crack initiation and propagation in Appendix A together with post-test surface topography show cracks forming and propagating in-line with deeper roughness scratches (or valleys) – see Figs. A2 and A3. Fig. 11 plots the measured average strain-to-failure on the outer tensile surface of the beam at mid-span against Ra (x). This calculation was based on the extension of a 6 mm line segment centred at mid-span on the outer surface – see Section 2.4. The perpendicular scratched cases (Ra 2.5, 5 & 10) and the polished case (Ra 0.009) (i.e. from Fig. 10) are shown connected by the dotted line, but two parallel scratched results (Ra 2.5 & Ra 10), the sandblasted result (Ra 4) and the 45° scratched result (Ra 10) are also included. It is important to note that all nominal roughness values given in the legend are, of course, measured across the scratches; whereas, the roughness on the x-axis refers to Ra (x) – roughness in the longitudinal tensile direction. Fig. 11 highlights the decreasing trend in strain-to-failure with increasing surface roughness. It also indicates that Ra (x) – i.e. roughness in the maximum tensile stress direction – is effective at capturing the trend as even the two parallel scratched cases and the sandblasted case follows the trend.

3.1.3. Effect of roughness orientation

Since the initial set of results in Fig. 8 pointed to the importance of surface feature orientation, a more focused comparison was carried out at a fixed roughness value. Fig. 12 plots the force-deflection curves for three different orientation instances of the Ra 10 μm unidirectional scratched surface (perpendicular: 90°, oblique: 45° and parallel: 0°) and Table 7 summarises the average deflection and work to failure. The figure confirms a significant sensitivity to scratch orientation. Parallel scratched samples can accommodate the most deformation, while perpendicular scratches are can accommodate significantly less and are clearly the most detrimental in terms of failure. This is likely to be because the perpendicular scratches are orientated perpendicular to the maximum tensile stresses in the bend samples (see Fig. 2): thus affording maximum tendency for crack opening. Table 7 quantifies the effect of moving from parallel to perpendicular scratches: the average deflection and work to failure drop by 1.6 and 1.7 times, respectively. Unsurprisingly, the result for the oblique 45° scratches lies in between the 0° and 90° results, but much closer to the 0° result indicating a non-linear relationship between deflection to failure and orientation.

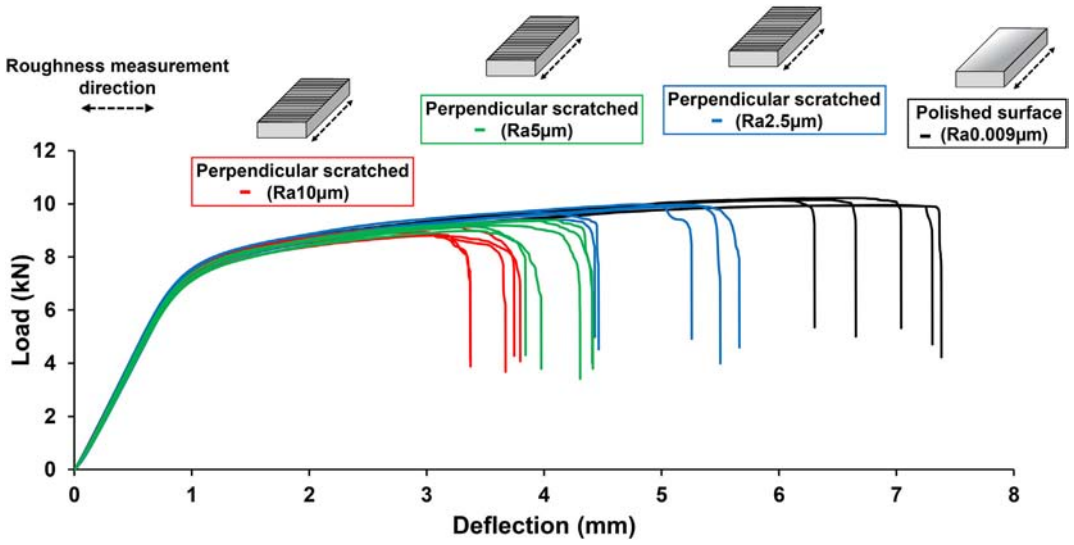

Fig. 10. Ti64 force-deflection curves for polished Ra 0.009 μm (black) and perpendicular scratched Ra 2.5, 5 and 10 μm (coloured blue, green & red, respectively). Five repeat results are shown for each. (For interpretation of the references to colour in this figure legend, the reader is referred to the web version of this article.)

Table 6
Max load, deflection to failure and work to failure (average over five repeat tests) for the Ti64 samples graphed in Fig. 10 (with measured mean roughness Ra & Sa). Plus/minus (±) values are standard deviations.

Surface condition	Ra (x) (μm)	Sa (μm)	Max load (kN)	Deflection to failure (mm)	Work to failure (J)
Perpendicular Scratched (Ra 10)	10	10	8.94 ± 0.12	3.59 ± 0.18	11,119.91 ± 2327.56
Perpendicular Scratched (Ra 5)	5	5	9.22 ± 0.15	4.19 ± 0.24	14,024.08 ± 179.76
Perpendicular Scratched (Ra 2.5)	2.44	2.62	9.74 ± 0.20	5.09 ± 0.56	20,508.08 ± 2591.33
Polished (Ra 0.009)	0.008	0.03	10.08 ± 0.12	6.94 ± 0.41	30,716.37 ± 1823.40

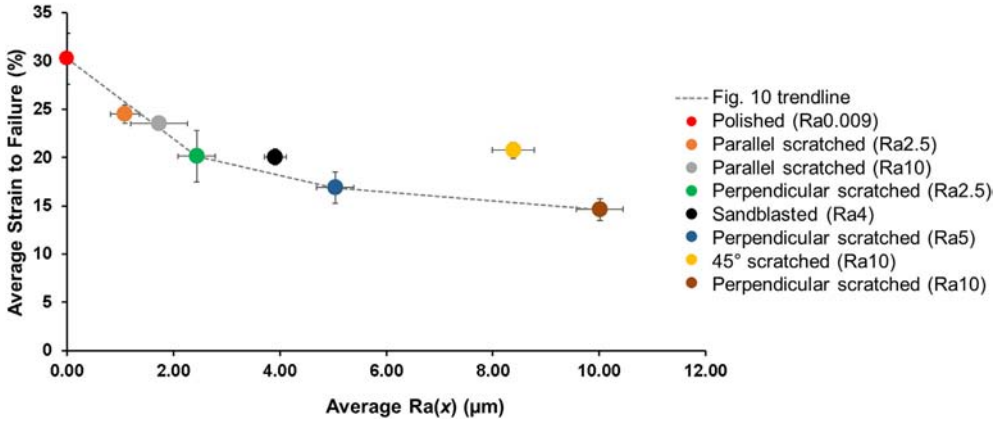

Fig. 11. Average measured strain-to-failure on the outer tensile surface at mid-span versus Ra (x) for Ti64. Each point is the average from five repeat tests. Average strain was determined for a 6 mm gauge length on the outer surface centred at mid-span as described in Section 2.4.

Fig. 12 indicates that failure initiation is likely to be more sensitive to orientations closer to 90°. Clearly, unidirectional roughness features (such as on a ground surface) lying perpendicular to significant tensile stress fields should be avoided.

Fig. 13 and Table 8 further confirm the importance of orientation. Fig. 13 compares the load-deflection curves for two instances of the parallel scratched surface having widely different nominal roughness magnitudes of 2.5 and 10 μm and Table 8 reports the average deflection and work to failure. It is clear that going from Ra 2.5 to Ra 10 μm has actually had almost no effect on the deflection and work to failure in this case. This is presumably because the maximum tensile stress in bending now acts nominally parallel to the scratches. The nominal roughness values (Ra 2.5 and Ra 10 μm) are, as outlined in Section 2.2, measured across the scratches; which for the parallel scratched case is the transverse or Ra(y) direction. If we look at the Ra(x) values (Table 8), on the other hand, we see that there is (as for the mechanical response in Fig. 13) little difference between the two surfaces. Therefore, the considerable difference in roughness in the transverse direction Ra(y) was unimportant as roughness in the Ra(x) direction (i.e. the direction of the maximum tensile stresses) appears to govern the relationship

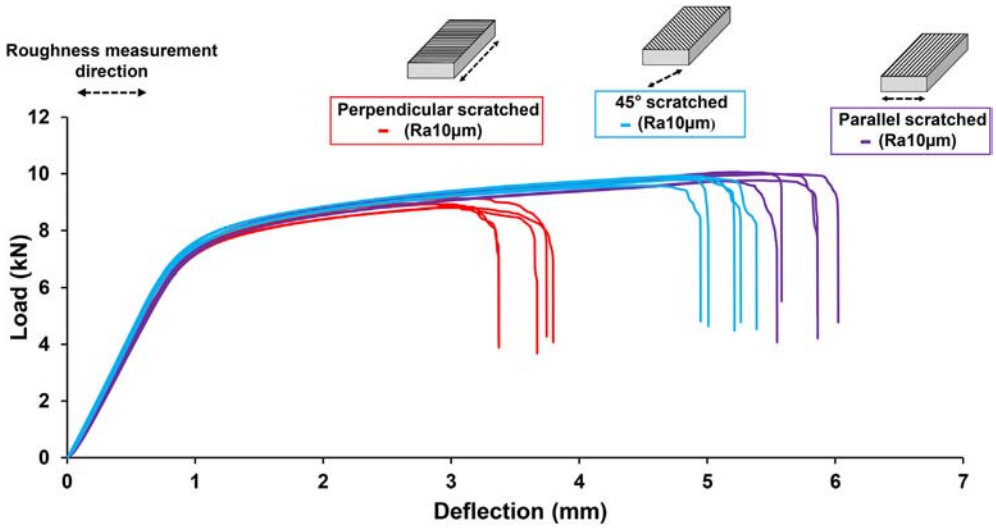

Fig. 12. Force-deflection curves for three different orientation instances (perpendicular: 90° (red), oblique: 45° (blue) and parallel: 0° (purple)) of the Ra 10 μm unidirectional scratched surface. Five repeat results are shown for each surface type (all Ti64). (For interpretation of the references to colour in this figure legend, the reader is referred to the web version of this article.)

Table 7
Max load, deflection to failure and work to failure (average over five repeat tests) versus scratch orientation for the Ti64 unidirectional scratched samples having roughness Ra = 10 μm across the scratches (i.e. graphed in Fig. 12). Plus/minus (±) values are standard deviations.

Scratch orientation	Max load (kN)	Deflection to failure (mm)	Work to failure (J)
Perpendicular	8.94 ± 0.12	3.59 ± 0.18	11,119.91 ± 2327.56
45°	9.81 ± 0.12	5.16 ± 0.16	16,983.22 ± 1638.36
Parallel	9.91 ± 0.13	5.79 ± 0.18	24,496.29 ± 1030.99

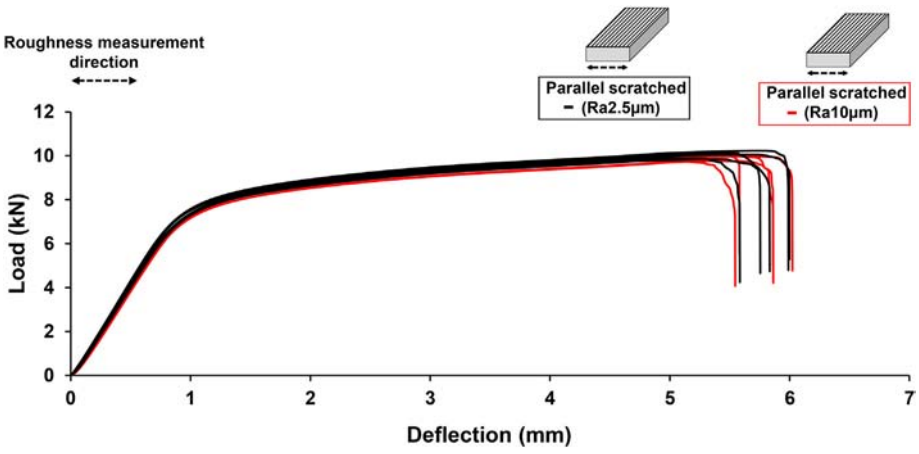

Fig. 13. Comparison of load-deflection curves for two widely separated roughness instances (Ra 2.5 and Ra 10 μm) of the unidirectional parallel scratched surface (both Ti64).

between roughness and failure. Fig. A4 in Appendix A shows that cracks propagate perpendicular to the roughness direction in this case (and hence, the depth of the roughness troughs are relatively unimportant in this scenario).

3.1.4. Ti64 overview

The conclusion from this section is that failure strain (and hence energy absorption) for Ti64 is highly sensitive to surface roughness (both magnitude and orientation). Failure strain drops off with increasing average surface roughness (if measured in the maximum tensile direction) and surface features orientated perpendicularly to tensile stresses are the most detrimental. This means that designers need to carefully consider the surface finish of safety-critical components and predictive models of failure will need to account for the effect. A reasonable question to ask at this point is whether residual stresses created during surface processing play a significant role. However, because rather low force surface processes were used here (i.e. sandblasting, abrading, polishing etc.) we assume that residual stress effects will be small. In any case, considering Fig. 12 where the same roughness (Ra = 10 μm) was imparted at different orientations it is unlikely that differences in residual stress fields could be responsible for the marked variation in deflection at failure. Also, in Fig. 13, going from Ra 2.5 to Ra

Table 8
Max load, deflection to failure and work to failure (average for five repeat tests) for Ti64 unidirectional parallel scratched samples having *nominal* roughness Ra = 2.5 and 10 μm (i.e. those graphed in Fig. 13). Measured mean roughness Ra & Sa also reported. Plus/minus (±) values are standard deviations.

Surface condition	Ra (*y*) (μm)	Ra (*x*) (μm)	Sa (μm)	Max load (kN)	Deflection to failure (mm)	Work to failure (J)
Parallel Scratched (Ra 10)	10.01	1.73	10	9.91 ± 0.13	5.78 ± 0.18	24,496.29 ± 1030.99
Parallel Scratched (Ra 2.5)	2.44	1.09	2.65	10.03 ± 0.14	5.83 ± 0.16	25,204.97 ± 1040.96

10 μm unidirectional scratched surfaces had almost no effect on failure strain when the scratches on each surface were orientated parallel to the longitudinal axis. If residual stress was a key factor, then we would expect to see a difference in failure strains over this range of scratch depths. We now consider the effect of roughness on the more ductile Ti407 alloy.

3.2. Ti407 results

Ti407 has considerably more ductility, but lower strength compared to Ti64. Sneddon et al. [12] found that strain-to-failure in tensile quasi-static testing of Ti407 was 60% higher than for Ti64, but the UTS was 34% lower. It is interesting to consider how this might affect the relationship between failure and surface roughness. To examine this further, a polished Ti407 sample (Ra 0.009) and three perpendicular scratched Ti407 samples having nominal roughness (across the scratches) of 2.5, 10 and 20 μm were tested. The resulting load-deflection curves are plotted in Fig. 14. In all cases, and even for the extreme roughness case of Ra = 20 μm, no failure occurred in three-point bending up to the maximum possible plunger displacement of 14 mm. Hence, the end of the plots in Fig. 14 represent where the test was stopped rather than material failure. In this case, we can say that even for the rather extreme deformation scenario here (see inset in Fig. 14), Ti407 is insensitive to a very wide range of surface roughnesses (i.e. Ra 0.009 to 20 μm). Table 9 gives the measured roughness values and the work expended in deforming to the terminal 14 mm deflection. Note that the energy absorbed here at the terminal deflection (average of 47.6 kJ) is already considerably greater than the longest straining Ti64 sample (polished) which absorbed 30.7 kJ before failing. It seems that the considerably higher ductility in Ti407 is sufficiently high to prevent failure due to propagation of a crack from the surface roughness features (i.e. essentially, the material can absorb the energy imparted without having to open a crack).

It is interesting that the two alloys (Ti64 and Ti407) behave very differently when it comes to sensitivity of failure to surface roughness. Namely: failure in Ti64 is highly sensitive to the surface roughness while Ti407 is completely insensitive (at least for the wide range of roughnesses Ra 0.009 to 20 μm examined here). This opens up the question of how various different materials might be assessed for the sensitivity of failure onset to surface roughness. Ultimately a predictive model is required which can describe failure for particular materials having prescribed surface topographies. This is perhaps a grand challenge, but in the next section, we develop a representative finite element model of some of the experimental roughness scenarios in order to better understand the link between roughness and failure.

4. Finite element model

We have seen above that the failure of Ti64 is strongly correlated with surface roughness. However, due to insufficient resolution of the optical image from the camera, it was difficult to pinpoint the exact locations where the cracks actually nucleate. This is an essential step in linking failure with surface roughness. In this section, a finite element (FE) model of the experimental three-point bend test was developed in ABAQUS in order to study the link between surface roughness features and crack nucleation. ABAQUS explicit is used to simulate a rigid roller in quasi-static frictionless normal contact with the Ti64 three-point bend sample which is supported by other two rigid rollers on the bottom surface (see Fig. 15). Dimensions are identical to the experiment.

The true measured roughness profiles with fine details down to the nanoscale (from the surface profilometer scans) were mapped onto a central region of the lower tensile boundary. A full 3D analysis would result in unrealistic solving time. Instead, the three-point bending test is simulated in the plane stress condition. Therefore, only the perpendicular scratched case from Section 3 is considered. Only the central region

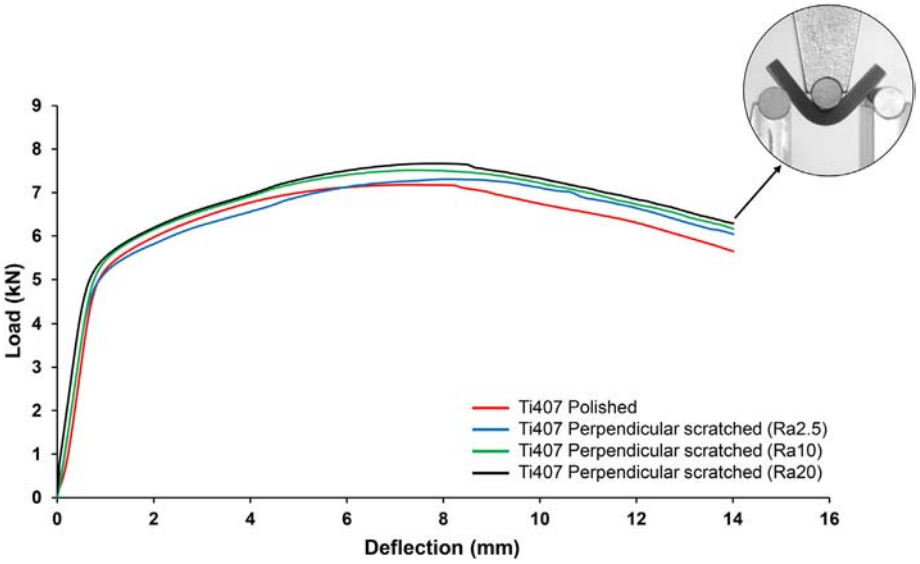

Fig. 14. Load-deflection curves for polished Ti407 (red) and perpendicular scratched samples of roughness Ra 2.5 μm (blue), Ra 10 μm (green) and Ra 20 μm (black). (For interpretation of the references to colour in this figure legend, the reader is referred to the web version of this article.)

Table 9
Measured mean roughness Ra & Sa, max load, deflection (14 mm for all samples) and 'work to 14 mm deflection' for all Ti407 samples (nominal designation: Polished Ra 0.009 and perpendicular scratched 2.5, 10 and 20 μm).

Surface condition	Ra (x) (μm)	Sa (μm)	Max load (kN)	Deflection (mm)	Work to 14 mm deflection (J)
Polished (Ra 0.009)	0.005	0.002	7.18	14.0	45,431.10
Perpendicular Scratched (Ra 2.5)	2.45	2.60	7.31	14.0	46,419.36
Perpendicular Scratched (Ra 10)	10	10	7.51	14.0	47,970.43
Perpendicular Scratched (Ra 20)	20	20	7.54	14.0	48,629.04

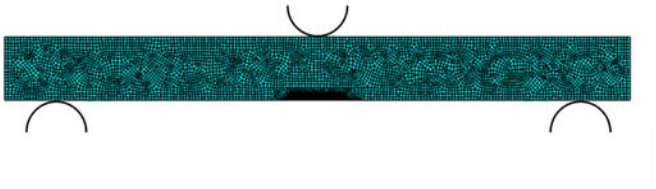

Fig. 15. An overview of the FE model.

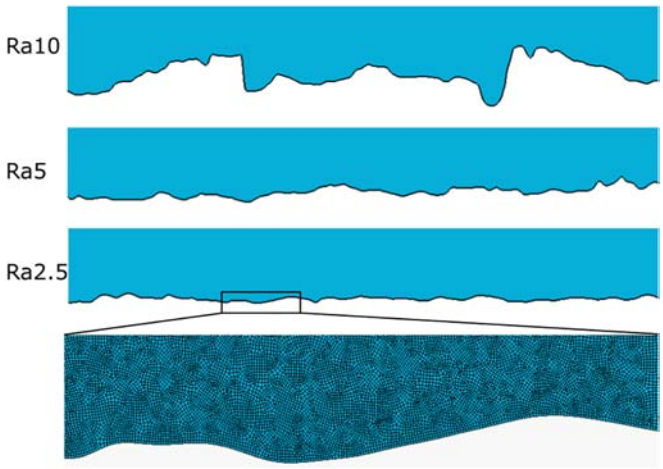

Fig. 16. Central 1 mm of mapped roughness for Ra 2.5, Ra 5 and Ra 10 μm. Lower expanded image is of a small region of the meshed Ra 2.5 μm roughness.

Table 10
Empirical parameters for the Johnson-Cook strength model.

A (MPa)	B (MPa)	N
928	1157.3	0.308

Table 11
Empirical parameters for the Johnson-Cook damage model [21].

d_1	d_2	d_2
−0.09	0.25	0.5

on the bottom edge with a width of 1 mm was mapped with roughness (since maximum tensile stresses in bending occur close to mid-span). Three perpendicular scratched cases were modelled: Ra = 2.5, Ra = 5 and Ra = 10 μm. Fig. 16 shows the central roughness region mapped into ABAQUS for each case. Quadrilateral and triangular elements, CPS4R and CPS3 were used. A thin layer right below the rough boundary is meshed using a quadrilateral element of size 500 nm. The coarsest mesh of size 0.25 mm is used for areas away from this thin layer.

A Johnson-Cook strength model

$$\sigma_p = A + B\,\epsilon_p^n$$

is used to simulate the elastoplastic deformation of Ti64 right before the damage is initiated. The empirical parameters are curve-fitted from the results of the uniaxial tensile test data in Sneddon et al. [12], see Table 10. All empirical parameters are consistent with published data in previous literature [24]. The Johnson-Cook damage model is used to identify the initial damage using the following critical value of equivalent plastic strain (PEEQ):

$$PEEQ_f = d_1 + d_2 \exp\left(d_3 \sigma_m / \sigma_v\right)$$

The corresponding damage evolution parameters used in the model are from [21] - see Table 11. Both material models are rate independent. The Young's modulus and Poisson's ratio of the Ti64 were 106.37 GPa and 0.342, respectively. The displacement-controlled damage evolution model is used to simulate crack nucleation and propagation in the fine layer with the finest element size. The crack occurs at the element if the corresponding maximum plastic displacement (starting from the necking) exceeds 49.75 nm and this critical value was obtained from uniaxial tensile tests. The reason why the damage evolution law is only limited within the fine layer is because the damage evolution model is element size-dependent. Therefore, the crack would falsely nucleate in the region with the coarsest mesh if the damage evolution model were applied to the entire FE model. On the other hand, it is unrealistic to map the entire sample using the 500 nm element size. Thus, as a compromise, the FE model is stopped before the surface cracks propagate through this thin layer. Mass scaling is used to increase the low stable time increment. Hourglass control is used to help relieve the element distortion in hourglass mode.

Crack nucleation occurred at an early stage of the three-point bending test for all three Ra values. The deflection (i.e. plunger displacement) at crack nucleation was 0.481, 0.284 and 0.248 mm, respectively for Ra = 2.5, 5 and 10 μm. The trend here is similar to the experiments: the crack nucleates at lower deflection values for rougher surfaces. The crack locations are highlighted by the red lines in Fig. 17. Multiple cracks are nucleated at the valleys of the roughness (the presence of multiple cracks was also observed experimentally – see Fig. A4 in Appendix A). This is a strong signal that crack nucleation is dominated by the local curvature of the roughness. Fig. 18. shows the roughness height, curvature and the corresponding equivalent plastic strain (PEEQ) distribution. The local maxima of the PEEQ are always correlated with the maxima of curvature and this strain concentration eventually triggers the crack nucleation at the same location (Fig. 19 shows an example of plastic strain concentration at valley tips). This is exactly like the model edge crack subjected to tensile stress. The larger the local curvature of the valley, the sharper the tip of the edge crack is and the greater the local stress intensity. Thus, considering surface roughness as a series of blunt crack-like features (Fig. 9) where the sharpness of the cracks (i.e. curvature of the roughness) is all-important in determining the likelihood of crack opening appears to be a satisfactory analogy. In the experiments, failure strain reduced with increasing Ra, but we can see visually from Fig. 5 that this also corresponds to increasing valley curvature.

We had already seen in Section 3 that Ra (x) (i.e. the average roughness in the tensile stress direction) was a good descriptor of failure

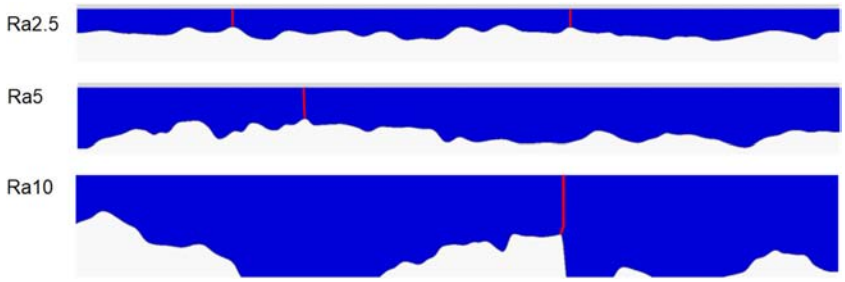

Fig. 17. Crack locations (highlighted by the red line). (For interpretation of the references to colour in this figure legend, the reader is referred to the web version of this article.)

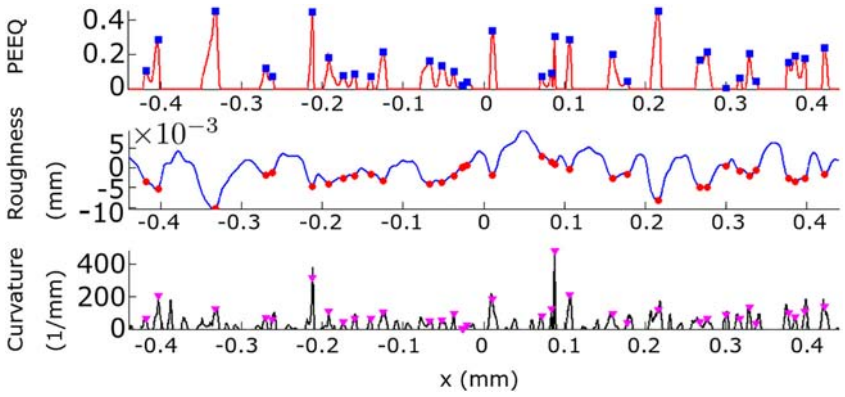

Fig. 18. Equivalent plastic strain, roughness height and curvature distribution. Horizontal axis is the longitudinal *x*-direction.

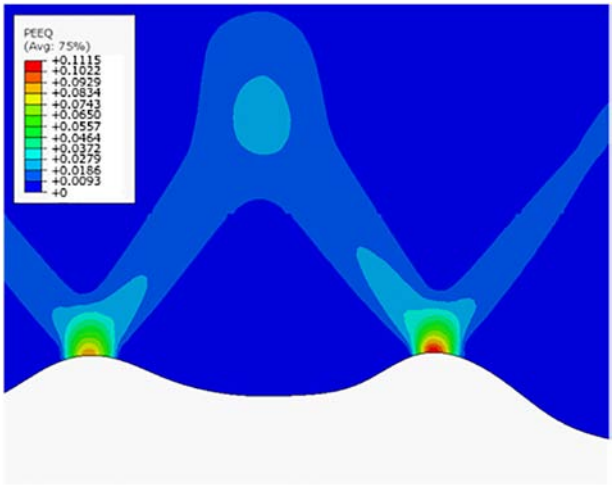

Fig. 19. PEEQ contour plot at the vicinity of a roughness valley prior to crack nucleation.

behaviour. Fig. 18, however, indicates that that valley surface curvature values are perhaps an even better descriptor as curvature directly indicates the sharpness of the cracks in the roughness-crack analogy. Although Ra and surface curvature are generally strongly correlated (i.e. greater amplitude often leads to greater curvature), one has to remember that Ra *only* includes amplitude information and therefore roughnesses with the same Ra can have different wavelengths and hence different curvatures. Therefore, a parameter such as the mean valley curvature (or mean curvature for the 10 most severe valleys in a region of interest) might be a more accurate descriptor when it comes to assessing the influence of particular surface topography on the initiation of failure.

5. Conclusions

A program of experiments was undertaken to study the effect of surface roughness on the failure of two titanium alloys: Ti64 and the more ductile Ti407. A series of surface topographies (polished, sandblasted and unidirectional scratched) was created over a deliberately wide range of surface roughness magnitudes ranging in Ra from 0.009 (polished) to 20 μm (rough scratched). The failure behaviour was investigated by testing rectangular beam samples in quasi-static three-point bending with the created surface topography imposed on the tensile beam surface. A finite element representation of the test (for the Ti64 perpendicular scratched samples) using the as-measured roughness profiles for the critical central portion of the tensile beam surface was also created.

For Ti64, failure was highly sensitive to surface roughness magnitude. Failure strain decreased with increasing average surface roughness (Ra) measured in the longitudinal beam direction. Going from the Ra 0.009 polished samples to the perpendicular scratched Ra 10 μm samples, the strain-to-failure dropped off by a factor of 2 and the work-to-failure reduced 2.7 times. Maximum load (and by extension, maximum stress) also decreased, but the effect was less significant as the strain hardening gradient is low in Ti64. The results were also highly sensitive to roughness orientation. For the unidirectional scratched samples, strain and work to failure dropped by factors of about 1.6 and 1.7, respectively, as the scratch orientation (for the same roughness) altered from 0 to 90° with respect to the longitudinal axis. However, going from Ra 2.5 to Ra 10 μm unidirectional scratched surfaces had almost no effect on failure strain when the scratches on each surface were orientated parallel to the longitudinal axis. In fact, the results indicated that it is the severity of the roughness in directions having significant surface tensile stress that matters. In three-point bending, the maximum tensile stress acts in the longitudinal beam direction; therefore, roughness in this direction governs failure. Thus, roughness features (i.e. scratches) perpendicular to appreciable tensile stress directions

are the most detrimental. The FE model of the Ti64 perpendicular scratched samples concluded that roughness valleys generating high curvature produced corresponding peaks in plastic strain and that cracks initiated at locations corresponding to the tips of these valleys. Therefore, surface roughness can be considered as a series of blunt crack-like features where greater crack tip curvature leads to higher stress intensity and a greater likelihood of crack propagation. Therefore, while average roughness (Ra) in the maximum tensile stress direction was found to be a good indicator of failure trends, a parameter based on surface curvature (in the same direction) may also be useful. Usually, Ra and surface curvature are well correlated, but Ra is an 'amplitude parameter' (i.e. does not distinguish changes in wavelength) so some surfaces can have equivalent Ra values, but different curvatures. A parameter such as average valley curvature or the average of the 10 most severe valley curvatures might be useful in assessing the failure-inducing tendency of surfaces. Although thought to play a minor role (compared to roughness magnitude and orientation) for the surface processes here, the effect of residual stresses produced during preparation of these surfaces is something that should be investigated further.

The mechanical responses obtained for Ti407 were completely insensitive to surface roughness (even up to the perpendicular scratched Ra = 20 μm case). This is because the alloy was too ductile to fail in the three-point bending setup even at very severe deformations. Clearly, the higher ductility of Ti407 means that more energy can be absorbed by material deformation as opposed to opening a crack from the surface roughness. This has to be noted as an advantage for Ti407 as insensitivity to surface roughness and surface defects means reduced machining and maintenance costs. The very different behaviour of Ti64 and Ti407 in relation to surface roughness requires further study. Ultimately, a predictive model capable of correctly describing failure for a particular material and surface topography is required.

Finally, the high sensitivity to surface roughness of the commonly used Ti64 alloy has very important implications. Many advanced models are available to predict failure of Ti64 based on bulk microstructural phenomenon, but if the surface roughness effect described here is ignored, these predictions (of failure strain or energy absorbed etc.) may be erroneous. For Ti64, designers need to carefully consider the surface finish on safety-critical components. Indeed for any metal alloy, the relationship between surface finish and failure should be considered in light of the above results. Presently, this requires mechanical testing in the absence of an integrated predictive model capable of accounting for both bulk and surface effects.

Data availability

Data related to the manuscript is available from the authors upon request and will be added to a University of Glasgow repository following publication (details available upon request).

Credit authorship statement

Scott Sneddon: Methodology, Conceptualization, Software, Validation, Formal analysis, Visualization, Investigation, Writing – Original draft. **Yang Xu:** Investigation, Formal Analysis, Software, Writing – Original draft. **Mark Dixon:** Supervision, Writing – Review and editing. **David Rugg:** Supervision, Writing – Review and editing, Project administration. **Peifeng Li:** Supervision, Conceptualization, Writing – Original draft, Writing – Review and editing, Project administration, Funding acquisition. **Daniel Mulvihill:** Supervision, Conceptualization, Writing – Original draft, Writing – Review and editing, Project administration, Funding acquisition.

Declaration of Competing Interest

The authors declare that they have no known competing financial interests or personal relationships that could have appeared to influence the work reported in this paper.

Acknowledgements

The authors would like to thank Dr. Andrew McBride of the University of Glasgow for useful discussions during the course of the work. They would also like to acknowledge the support of Rolls-Royce plc and the University of Glasgow for funding the work (including a PhD studentship for the first author). Scott Sneddon would like to thank Dr. Zhe Liu for assistance in bend rig design and technician Thomas Dickson for assistance in manufacture. The bend rig design is adapted from that developed by Dr. Liu in Refs [25, 26].

Appendix A

Here, we look more closely at crack initiation and development and how this relates to surface roughness. For the Ti64 samples with Ra = 10 μm, we have completed some experiments where we also capture a video of the middle of the lower tensile surface in-situ during the bend tests. A 3D printed 45° block was printed and a mirror was attached as shown in Fig. A1. The mirror was positioned at the underside of the rough surface and a Pixelink camera captured images at 300fps during the test (via the mirror)

An image of a perpendicular scratched surface with an inverted contrast is shown in Fig. A2. Fig. A2(a) is the unloaded specimen and also shows a deeper perpendicular scratch on the left side of the specimen (highlighted in yellow). During the test (Fig. A2(b–c)) we see that the crack initiation and propagation also coincides with the location of the deeper scratch (i.e. left half of specimen). The image prior to failure is shown in Fig. (c). This observation confirms our assertion that crack initiation is dictated by the most severe roughness valleys (i.e. deepest scratches with highest curvature).

Fig. A3 shows two post-test 3D surface scans for perpendicular scratched Ti64 (measured using an Alicona 3D surface profilometer). The scans are taken at mid-span on the tensile beam surfaces and show the detrimental cracks present. In Fig. A3(a), a single detrimental crack developed while in Fig. A3(b), a pair of detrimental cracks formed. These two modes where roughly equally observed in the samples tested. Both scans again confirm that crack location and orientation coincide with the surface roughness features – the arrows in Fig. A3(b) point to the roughness features (deep perpendicular scratches) from which the cracks emerged.

In-situ imaging (of the tensile surface at mid-span) was also conducted on a parallel scratched surface as shown in Fig. A4. Here the images confirm that roughness perpendicular to the maximum tensile stresses is less important since the crack does not propagate along the roughness valleys in this case (as the maximum tensile stress direction is now perpendicular to the roughness valleys). In Fig. A4, multiple crack initiation sites are visible, thus agreeing with the modelled predictions in Section 4.

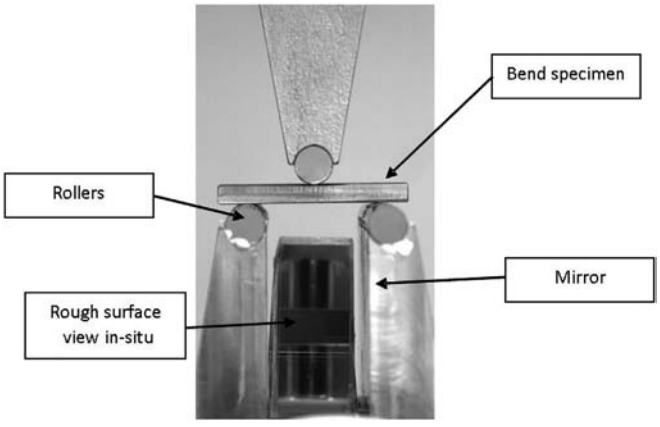

Fig. A1. Setup for *in-stiu* imaging of crack formation and propagation at the middle of the lower tensile specimen surface during three-point bend tests.

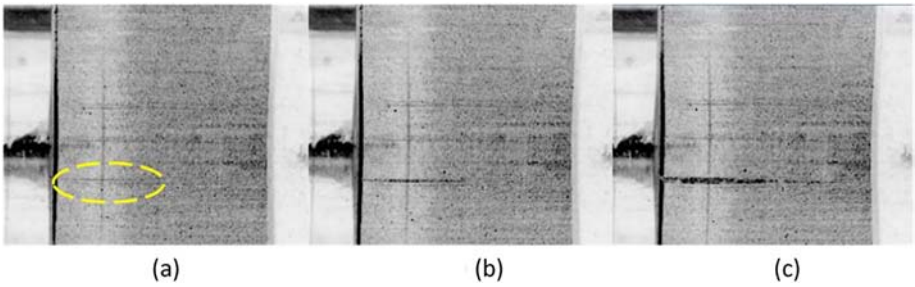

Fig. A2. Evolution of surface crack at middle of lower tensile surface in Ti64 perpendicular scratched samples (Ra 10 μm): (a) Unloaded case with deep roughness scratch highlighted in yellow, (b) mid-test showing crack propagation coinciding with the deep scratch location and (c) an image just prior to catastrophic failure. (For interpretation of the references to colour in this figure legend, the reader is referred to the web version of this article.)

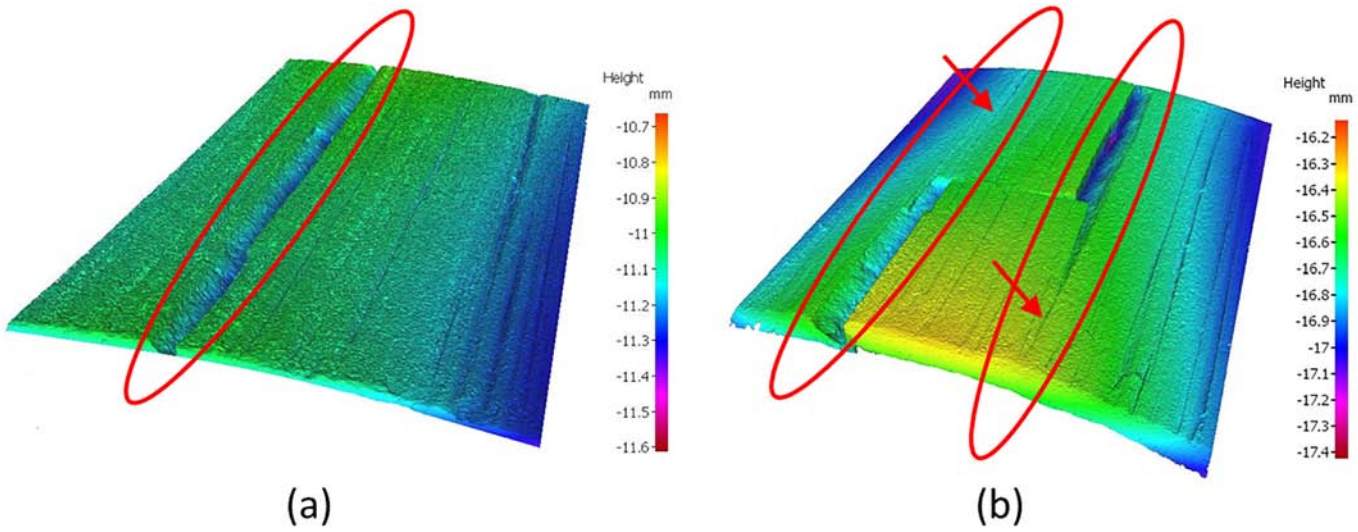

Fig. A3. Ti64 (Perpendicular scratched) post-test 3D surface scans of the tensile beam surface at mid-span indicating how crack location and direction follows the roughness scratches: (a) a single detrimental crack (Ra = 10 μm case) and (b) the development of a pair of detrimental cracks (Ra = 5 μm case). Note, after removal of the load, the specimens are not fully fractured and some spring-back tending to close the cracks occurs – hence the images seen here. The arrows in (b) indicate the roughness feature from which the crack developed. Scans are full specimen width.

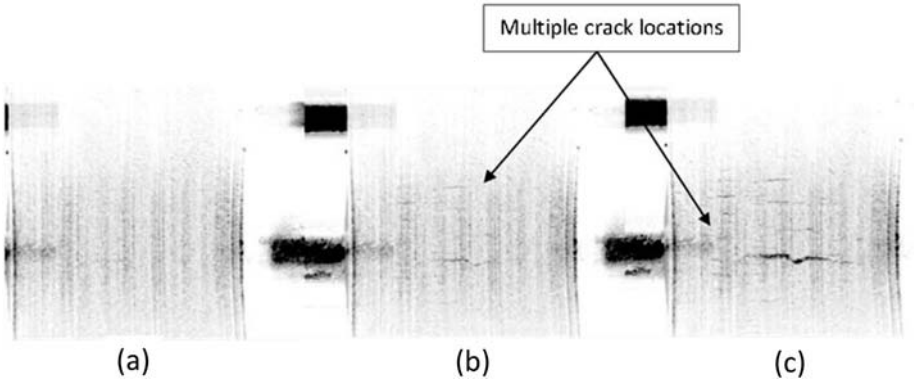

Fig. A4. Evolution of surface cracks at middle of lower tensile surface in Ti64 parallel scratched samples (Ra 10 μm): (a) Unloaded case, (b) mid test showing multiple crack initiation sites and (c) an image just prior to catastrophic failure again indicating the presence of multiple cracks.

References

[1] G. Lütjering, J.C. Williams, Titanium, Springer Berlin Heidelberg, 2007.
[2] C. Leyens, M. Peters, Titanium and Titanium Alloys: Fundamentals and Applications, Wiley, 2006.
[3] A. Hasçalık, U. Çaydaş, A comparative study of surface integrity of Ti–6Al–4V alloy machined by EDM and AECG, J. Mater. Process. Technol. 190 (1) (2007) 173–180.
[4] R. Bertolini, L. Lizzul, L. Pezzato, A. Ghiotti, S. Bruschi, Improving surface integrity and corrosion resistance of additive manufactured Ti6Al4V alloy by cryogenic machining, Int. J. Adv. Manuf. Technol. 104 (5) (2019) 2839–2850.
[5] J.T. Philip, J. Mathew, B. Kuriachen, Tribology of Ti6Al4V: A review, Friction 7 (6) (2019) 497–536.
[6] M.J. Donachie, Titanium: A Technical Guide, 2nd Edition, ASM International, 2000.
[7] P.K. Kaway, X. Zhang, Experimental study on surface integrity of titanium alloy Ti6Al4V by ball end milling, J. Inst. Eng. (2018) 115–121.

[8] S. James, Y. Kosaka, R. Thomas, P. Garratt, Timetal® 407: A titanium alloy to enable cost reduction, Proceedings of the 13th World Conference on Titanium, Wiley 2020, pp. 721–725.
[9] Y. Millet, S. James, Y. Kosaka, R. Thomas, P. Garratt, Timetal® 407: A titanium alloy to enable cost reduction, Proceedings of the 13th World Conference on Titanium, Wiley, 2016.
[10] A. Fitzner, M. Thomas, J.Q.D. Fonseca, S.-Y. Zhang, J. Kelleher, M. Preuss, The effect of aluminium on deformation and twinning in alpha titanium: the ND case, Proceedings of the 13th World Conference on Titanium 2016, pp. 1051–1055.
[11] Z. Kloenne, G. Viswanathan, M. Thomas, M.H. Lorreto, H.L. Fraser, A comparative study on the substructure evolution and mechanical properties of TIMETAL®407 and Ti-64, The 14th World Conference On Titanium, 321, MATEC Web Conf. 2019, p. 11045.
[12] S. Sneddon, M.D. Mulvihill, E. Wielewski, M. Dixon, D. Rugg, P. Li, Deformation and failure behaviour of a titanium alloy Ti-407 with reduced aluminium content: a comparison with Ti-6Al-4V in tension and compression, Materials Characterization (2021) In press.
[13] L. Pazos, P. Corengia, H. Svoboda, Effect of surface treatments on the fatigue life of titanium for biomedical applications, J. Mech. Behav. Biomed. Mater. 3 (6) (2010) 416–424.
[14] M. Dumas, et al., Influence of the finish cutting operations on the fatigue performance of Ti-6Al-4V parts produced by selective laser melting, Procedia CIRP 71 (2018) 429–434.
[15] M.R. Bayoumi, A.K. Abdellatif, Effect of surface finish on fatigue strength, Eng. Fract. Mech. 51 (5) (1995) 861–870.
[16] D. Novovic, R.C. Dewes, D.K. Aspinwall, W. Voice, P. Bowen, The effect of machined topography and integrity on fatigue life, Int. J. Mach. Tools Manuf. 44 (2) (2004) 125–134.
[17] P.S. Maiya, D.E. Busch, Effect of surface roughness on low-cycle fatigue behavior of type 304 stainless steel, Metall. Trans. A. 6 (9) (1975) 1761.
[18] H. Itoga, K. Tokaji, M. Nakajima, H.N. Ko, Effect of surface roughness on step-wise S–N characteristics in high strength steel, Int. J. Fatigue 25 (5) (2003) 379–385.
[19] M. Knezevic, et al., Modeling bending of α-titanium with embedded polycrystal plasticity in implicit finite elements, Mater. Sci. Eng. A 564 (2013) 116–126.
[20] M.A. Galindo-Fernández, K. Mumtaz, P.E.J. Rivera-Díaz-del-Castillo, E.I. Galindo-Nava, H. Ghadbeigi, A microstructure sensitive model for deformation of Ti-6Al-4V describing cast-and-wrought and additive manufacturing morphologies, Mater. Des. 160 (2018) 350–362.
[21] W.J. Harrison, M.T. Whittaker, R.J. Lancaster, A model for time dependent strain accumulation and damage at low temperatures in Ti–6Al–4V, Mater. Sci. Eng. A 574 (2013) 130–136.
[22] Y. Chong, G. Deng, S. Gao, J. Yi, A. Shibata, N. Tsuji, Yielding nature and hall-Petch relationships in Ti-6Al-4V alloy with fully equiaxed and bimodal microstructures, Scr. Mater. 172 (2019) 77–82.
[23] D. Lunt, The Effect of Macrozones in Ti-6Al-4V on the Strain Localisation Behaviour, The University of Manchester, Manchester, 2014.
[24] D. Lesuer, Experimental Investigation of Material Models for Ti-6Al-4V and 2024-T3, 2000.
[25] Z. Liu, 'Evaluation of 3D Failure Modes in CFRP Composites Laminates', PhD Thesis, Nanyang Technological University, Singapore, 2016.
[26] Z. Liu, P. Li, N. Srikanth, T. Liu, G.B. Chai, Quantification of flexural fatigue life and 3D damage in carbon fibre reinforced polymer laminates, Comp. Part A 90 (2016) 778–785.